ACS NANO

www.acsnano.org

ARTICLE

Refractive Index Sensing for Measuring Single Cell Growth

Arif E. Cetin,* Seda Nur Topkaya, Ozden Yalcin-Ozuysal, and Ali Khademhosseini

Cite This: *ACS Nano* 2021, 15, 10710–10721

Read Online

ACCESS | Metrics & More | Article Recommendations | Supporting Information

ABSTRACT: Accessing cell growth on adhesive substrates is critical for identifying biophysical properties of cells and their therapeutic response to drug therapies. However, optical techniques have low sensitivity, and their reliability varies with cell type, whereas microfluidic technologies rely on cell suspension. In this paper, we introduced a plasmonic functional assay platform that can precisely measure cell weight and the dynamic change in real-time for adherent cells. Possessing this ability, our platform can determine growth rates of individual cells within only 10 min to map the growth profile of populations in short time intervals. The platform could successfully determine heterogeneity within the growth profile of populations and assess subpopulations exhibiting distinct growth profiles. As a proof of principle, we investigated the growth profile of MCF-7 cells and the effect of two intracellular metabolisms critical for their proliferation. We first investigated the negative effect of serum starvation on cell growth. We then studied ornithine decarboxylase (ODC) activity, a key enzyme which is involved in proliferation, and degraded under low osmolarity that inhibits cell growth. We successfully determined the significant distinction between growth profiles of MCF-7 cells and their ODC-overproducing variants that possess strong resistance to the negative effects of low osmolarity. We also demonstrated that an exogenous parameter, putrescine, could rescue cells from ODC inhibition under hypoosmotic conditions. In addition to the ability of accessing intracellular activities through *ex vivo* measurements, our platform could also determine therapeutic behaviors of cancer cells in response to drug treatments. Here, we investigated difluoromethylornithine (DFMO), which has antitumor effects on MCF-7 cells by inhibiting ODC activity. We successfully demonstrated the susceptibility of MCF-7 cells to such drug treatment, while its DFMO-resistant subpopulation could survive in the presence of this antigrowth agent. By rapidly determining cell growth kinetics in small samples, our plasmonic platform may be of broad use to basic research and clinical applications.

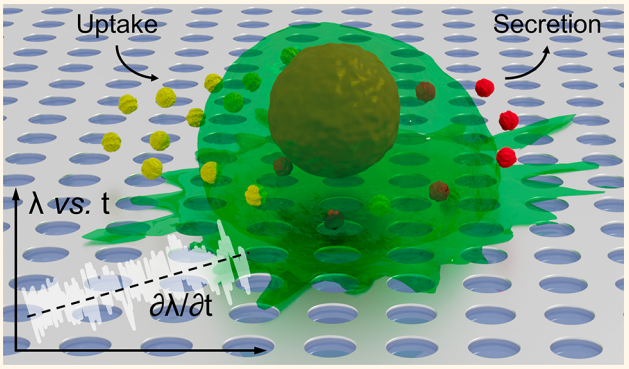

KEYWORDS: *plasmonics, label-free biosensing, cell-growth profiling, functional assays, cellular metabolism, nanohole arrays*

Uptake or secretion of molecular contents plays an important role for cell growth. Classically, *ex vivo* studies, investigating cellular pathways that are related to cell growth, mainly rely on monitoring bulk cell populations over long periods, where the individual cell responses are averaged. On the other hand, cellular response at the single-cell level to an external stimulus determined within a very short time interval could give more accurate information related to dynamic cellular activities. Moreover, single cells with different growth profiles could be a sign of biochemical or biophysical differences within the population of interest. For example, small subpopulations in cancer models could show dramatic resistance in standard-of-care drugs.[1] However, such distinct variations related to minor groups are difficult to determine in population-based studies.

Currently, optical and microfluidic approaches are used to monitor single cell growth. In the first method, cell growth is determined based on the change in the cell volume, where microscopic images of cells are used. A 2-dimensional cell image and the cross-section that is determined based on different assumptions, *e.g.*, constant height or oval shape, are used to calculate the volume. However, these assumptions can be applicable to few cell types but mostly cannot be used reliably even within the same populations, which present

Received: May 12, 2021
Accepted: May 17, 2021
Published: May 24, 2021

https://doi.org/10.1021/acsnano.1c04031
ACS Nano 2021, 15, 10710–10721

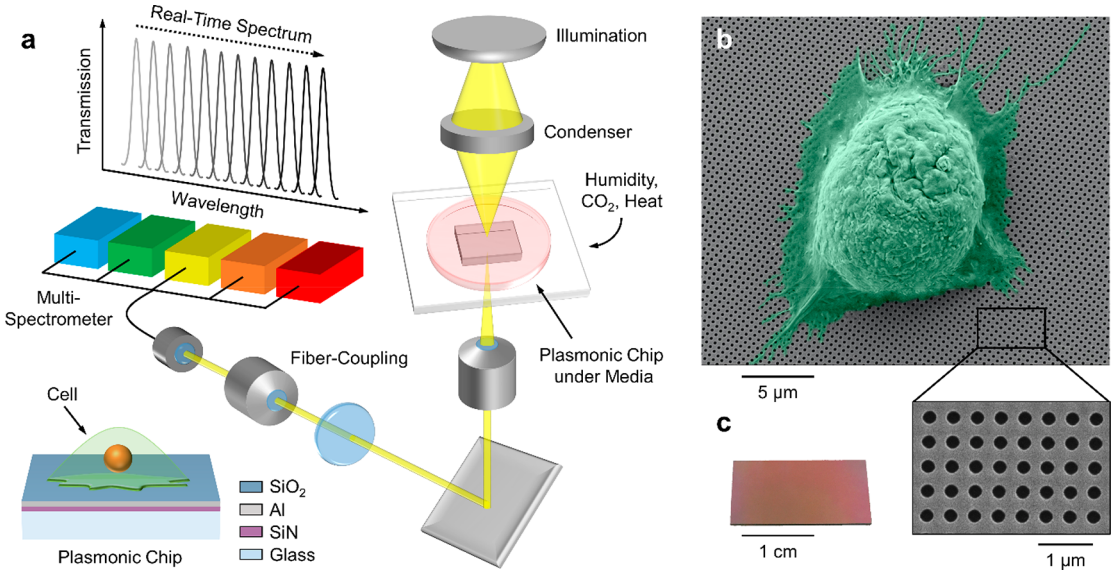

Figure 1. Plasmonic cell-growth profiling platform. (a) Schematic illustration of the cell-growth profiling platform that employs a sensitive spectral read-out scheme to dynamically determine accumulated mass by cells *via* monitoring the transmission response of a plasmonic chip. Cells are seeded on the plasmonic chip, composed of a thin Al film that is textured with periodic nanohole arrays. The film stands on a glass substrate with a SiN interlayer in between. The surface of the Al film is covered with a SiO_2 layer. (b) SEM image of an MCF-7 cells adhered on the surface of the plasmonic chip. (c) Photo (left) and SEM image (right) of the plasmonic chip.

irregularities.[2] Also, quantitative phase microscopy is used to determine cells' dry mass.[3] However, this method is not easily applicable to different cell types. Recently, a suspended microchannel resonator technology has been introduced for measuring cell mass with much higher precision compared to former approaches.[4] While this approach is effective for cell suspensions, it has inherent limitations for adherent cells as it requires trypsinization.

One potential way to address these limitations could be through the use of plasmonics. Previously, plasmonic platforms have been used to identify different target analytes, from small biomolecules, *e.g.*, protein,[5] to large organisms, *e.g.*, bacteria[6] or virus,[7] in a label-free fashion due to the special surface electromagnetic waves called surface plasmons (SPs). Despite their strong optical properties, this label-free biosensing technology has not been fully investigated to identify biophysical properties of cells or their therapeutic behavior. So far, there have been several cell-oriented studies on optical, chemical, and biological techniques adapted for label-free plasmonic technologies. In some of these studies, molecules involved in cellular pathways were detected, *e.g.*, extracellular proteins.[8] Plasmonic substrates were also used to investigate the dynamics of cell attachment and to guide cellular behaviors using plasmonic properties.[9,10] Plasmonic structures could also be used to study extracellular proteins that could be critical for cancer diagnostics or treatment.[11] Employing plasmonic platforms, levels of secreted factors could be detected, which could be used to characterize single-cell signaling for basic and clinical research.[12,13] Therefore, in the literature, for the plasmonic platforms, which monitor spectral variations within the plasmonic responses due to the secreted molecules captured by the ligands on the sensor surface, there is no direct contact between cells and the plasmonic substrate. On the other hand, the studies that rely on the direct contact mainly investigate the state of the cell adhesion on the sensor surface by monitoring plasmonic variations upon the cell attachment or detachment. Hence, the link between accumulated mass by cells on plasmonic substrates and how it dynamically effects plasmonic responses have not been investigated yet.

In this paper, we introduce a plasmonic platform that could be a strong alternative to optical and microfluidic technologies for measuring cell growth. In this approach, the change in the cell mass is determined by monitoring its effective refractive index in the vicinity of the surface of the plasmonic substrate. The relationship between cell growth and the accumulated mass by the cell was determined from the spectral variations observed within the optical response of the plasmonic substrate. The platform could provide precise mass data from cells seeded on a sensing surface, promoting their adhesion without the need for a sample preparation step, under a cell culture environment. By adding/subtracting a stimuli or a molecular/therapeutic agent, the platform could determine susceptibility or resistance of cells to the external effects by monitoring the variations in their growth profile.

RESULTS AND DISCUSSION

Working Principle of the Cell-Growth Profiling Platform. The platform utilizes a sensitive plasmonic chip, based on periodic nanohole arrays fabricated through a 120 nm thick aluminum film (Al), to determine dynamic changes within the cell mass (see the Methods for the details of the plasmonic chip). Nanohole arrays use the combination of localized and propagating SPs, *i.e.*, they excite a plasmonic mode associated with large local electromagnetic fields concentrated at the Al surface, and extensively extend within the medium in the vicinity of the plasmonic surface, ensuring strong sensitivities to changes in the effective refractive of the medium.[14] Figure 1a shows the schematic illustration of the optical setup utilized for growth profiling measurements. The platform has a high spectral resolution, *e.g.*, 0.9 Å, which is critical to determine small changes in the cell mass (see the Methods for the experimental setup). The platform ensures healthy cell proliferation by integrating to a cell culture

https://doi.org/10.1021/acsnano.1c04031
ACS Nano 2021, 15, 10710−10721

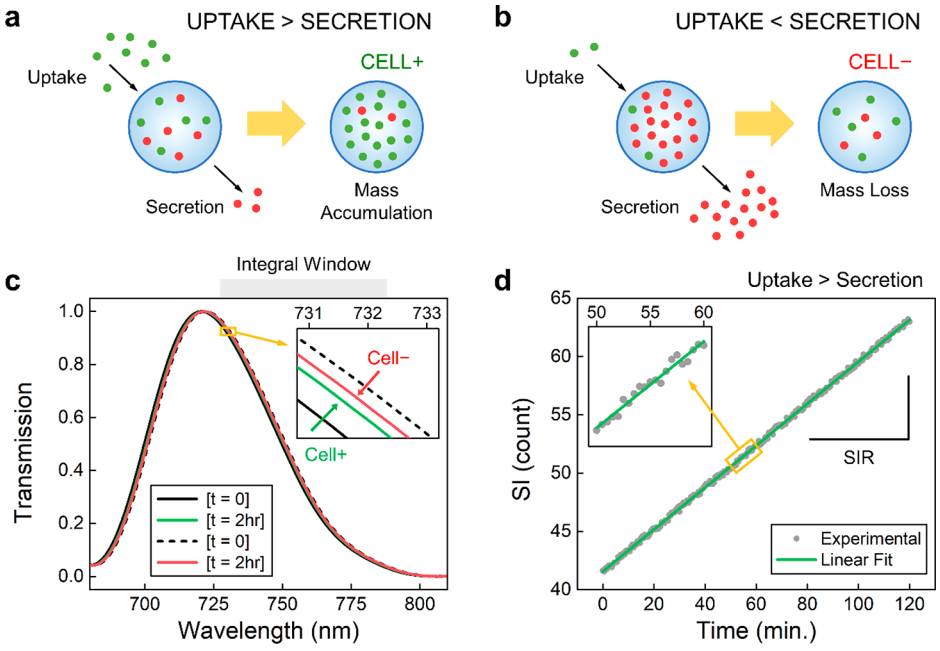

Figure 2. Uptake or secretion of molecules determines cell-growth rate. Schematic illustration of a cell where (a) the cellular uptake exceeds secretion, *i.e.*, the cell mass increases *via* molecular accumulation, and (b) the cellular secretion exceeds uptake, *i.e.*, the cell mass decreases *via* molecular loss over time. (c) Transmission resonance of the nanohole arrays seeded with cells gaining (Cell+) and losing (Cell−) mass. For Cell+, transmission resonance red-shifts upon the accumulated mass during the 2 h long measurement, *e.g.*, solid black (t = 0) to green (t = 2 h). For Cell−, transmission resonance blue-shifts upon the mass loss during the 2 h long measurement, *e.g.*, dashed black (t = 0) to red (t = 2 h). The figure inset shows the 2.4 nm wide zoomed spectrum, highlighting the multiple spectral shifts in different wavelengths within the transmission resonance. (d) SI values (gray dots) calculated over a 2 h long seeding time for a cell accumulating mass. SI value was calculated with the integral of the transmission resonance values within the integral window denoted with the gray box in Figure 2c. Figure inset shows the 10 min long zoomed region, demonstrating the same SIR with the 2 h long measurement. For each cell, SIR was calculated from the slope of the linear least-squares fitted (green curve) to the SI *vs* time data.

incubator. Figure 1b shows the scanning electron microscopy (SEM) image of the nanohole arrays, where a single human MCF-7 cell was adhered on the Al surface (see the Methods for the cell culture preparation). Plasmonic chips were fabricated through a high-throughput manufacturing technique based on deep-ultraviolet lithography (see the Methods for the fabrication of the plasmonic chips). Figure 1c (left) shows the photo of the plasmonic chip with 2 cm × 1 cm dimension. Nanoholes have a diameter of 240 nm, and the periodicity of the array is 450 nm. Figure 1c (right) shows the SEM image of the nanohole arrays, demonstrating their uniformity. This structural uniformity is very critical for our growth-profiling platform as it provides surface waves uniformly distributed over the sensing surface, which ensures a fair evaluation of cells on the same plasmonic surface since the plasmonic responses are identical at the background and each sensor location where different cells are under measurement.

Parts a and b of Figure 2 show the schematic illustration of the two scenarios, where (i) the cellular uptake exceeds secretion (green and red circles represent the absorbed and secreted molecules, respectively), *i.e.*, net mass increases by the accumulation over time, and (ii) the cellular uptake is lower than secretion, *i.e.*, the cell loses mass. Under the cell medium, nanohole arrays excite a transmission resonance at ∼699 nm with ∼51 nm line width (see Supporting Figure S1 for the details of the plasmonic mode of interest). In Figure 2c, we show the data corresponding to two individual cells, *e.g.*, cells gaining (Cell+) and losing (Cell−) mass. Attachment of cells on the plasmonic surface dramatically increases the effective refractive index, which shifted the transmission resonance to ∼720 nm for Cell+ (solid black curve) and ∼722 nm for Cell− (dashed black curve). The initial position of the transmission resonance corresponding to the sensor locations, where Cell+ and Cell− were seeded, is the same since our fabrication technique ensures identical nanohole features throughput the chip surface. Therefore, this 2 nm spectral difference (720 nm *vs* 722 nm) between the transmission responses for Cell+ and Cell− could be due to their mass difference, *e.g.*, mass(Cell−) > mass(Cell+). In our platform, cells were seeded on the chip surface 24 h prior to the growth profiling tests (see the Methods for chip preparation for cell seeding) in order to eliminate spectral variations due to dynamic adhesion of cells which were initially in suspension. Accumulated mass increases the effective refractive index and shifts the transmission resonance to longer wavelengths (green), while the mass loss decreases the effective refractive index, shifts the transmission resonance to shorter wavelengths (red). Despite its highly sensitive character to the analyte binding on the sensing surface,[15] transmission resonance shifted by only ∼0.8 nm (Cell+) and ∼0.4 nm (Cell−) within the period of 2 h. Such small spectral variations could be due to the small mass changes with a mass accumulation rate in ∼ pg/h level,[4,16] which create small refractive index changes on the sensing surface. In order to compensate for this drawback, we utilized a highly sensitive plasmonic chip and an optical read-out scheme with a high spectral resolution. Using this very sensitive label-free biodetection platform, we have previously detected thin protein layers with a sub-1 ng/mL detection limit.[15] In the classical technique, spectral variations are monitored only at the transmission resonance (spectral position of the trans-

https://doi.org/10.1021/acsnano.1c04031
ACS Nano 2021, 15, 10710−10721

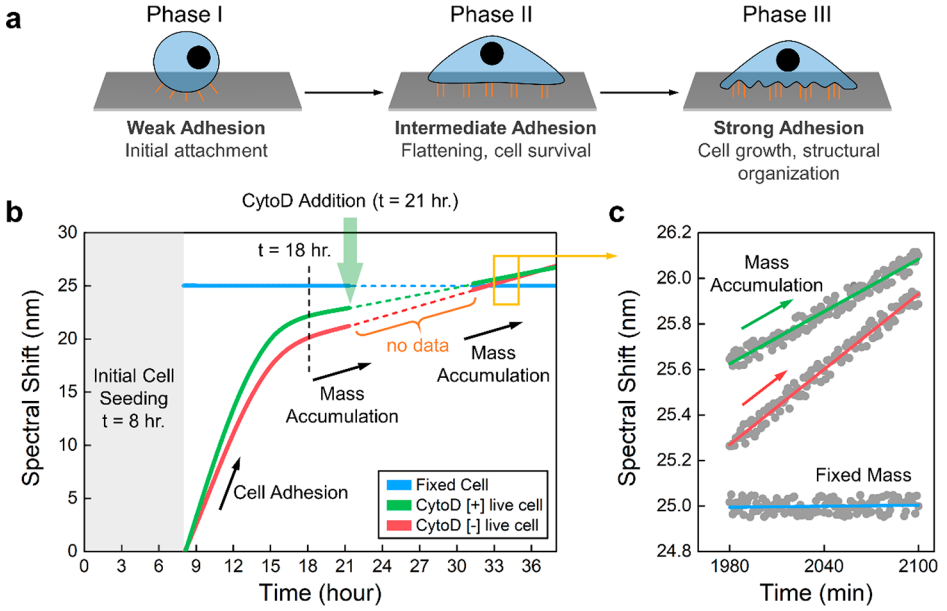

Figure 3. Cell migration does not alter growth-profiling measurements. (a) Schematic illustration of cell adhesion phases. (b) Spectral shift within the transmission resonance of the nanohole arrays for a 38 h long period. Cells were seeded on the chip surface t = 8 h prior to the measurements. At t = 18 h, behavior of the spectral shifts shifted from exponential to linear. At t = 21 h, 10 μM CytoD was added to the cell media for the cell denoted with green. The cell seeded in the normal media and the formalin-fixed cell are denoted with red and blue, respectively. Spectral measurements were restarted 10 h after the addition of CytoD (t = 31 h). (c) 2 h long zoomed region, showing the spectral variations due to formalin-fixed (blue), CytoD [+] (green), and CytoD [-] (red) cells.

mission maxima). To further improve the sensitivity of our platform, we implemented a postprocessing technique that could consider the collective behavior of spectral variations around the transmission resonance. Figure 2c (inset) shows a 2.4 nm wide spectral window within the transmission resonance, which demonstrates the collective shifts in different wavelengths for Cell+ (solid black to green) and Cell− (dashed black to red). In order to consider these multiple variations, we integrated the transmission values in a 60 nm wide spectral window denoted with a gray box in Figure 2c. For plasmonic biosensors, the largest spectral shifts occur for the wavelengths, where light-matter interaction is the strongest; *i.e.*, we positioned the integral window very close to the transmission resonance. The position of the spectral integral window is critical to provide reliable population-level information. In order to consider the Lorentzian shape of the transmission resonance, and having the fact that the transmission resonance shifted by sub-1 nm within a 2 h long measurement, we positioned the spectral window at 727 nm. This wavelength is longer than the spectral position of the transmission maxima in the beginning and at the end of the growth measurements for all cells used in the population test. Hence, only the transmission values of the spectral shoulder on the right side of the transmission resonance were used, while the spectral shoulder on left side was excluded for the calculations. This prevents any miscalculation due to the Lorentzian shape of the transmission resonance.[17]

Accumulated mass red-shifts the transmission resonance, which increases its overlap with the integral window and, thus, increases the calculated value. On the other hand, mass loss decreases the integral value by further mismatching the transmission resonance and the integral window. Figure 2d shows the change in the spectral integral (SI), where the transmission response was measured at every 30 s over the course of 2 h. The figure demonstrates the consistent increase in the SI value, which could be attributed to the accumulated mass by the cell. In our method, cell mass is represented by SI, *i.e.*, the rate of change within the cell mass is determined by the spectral integral rate (SIR). Here, SIR is directly related to the mass accumulated or lost by a cell over time and calculated by the slope of the linear least-squares fitted to the SI *vs* time data. This consistent growth behavior over a long period of time enables us to study the cellular behaviors over a much shorter duration. For example, as shown in Figure 2d (inset), we performed growth profiling measurements over 10 min, which provides the same SIR value with the 2 h long measurement. Performing growth-profiling tests of single cells within such short period of time could increase the throughput, which is critical to determine population behaviors whose reliability relies on the number of cells. Furthermore, the ability of rapid profiling could eliminate any optical or mechanical fluctuations within the transmission resonance due to long test durations.

In our plasmonic platform, accumulated mass by cells on the Al surface is determined by a sensing-by-binding based detection technique. Thus, a rigid adhesion of cells on the sensing surface is critical to reliably track mass change in real-time. As we stated previously, seeding cells 24 h prior to the measurements eliminated the spectral variations due to the attachment or detachment in the formation of adherent cells from suspension. A second possible spectral contribution could be cell migration. Therefore, in this section, we investigated the effect of cell migration on growth profile calculations. Figure 3a shows the schematic illustration of cell adhesion phases (see the Supporting Information for details of cell adhesion phases). In order to determine the effect of cell migration on the effective refractive index in the vicinity of the sensor location occupied with a single cell, we compared the spectral variations associated with two cells, one dosed with 10 μM cytochalasin D (CytoD) in Figure 3b. CytoD is an inhibitor of actin polymerization, and it inhibits cell migration.[18] Since in Phase

https://doi.org/10.1021/acsnano.1c04031
ACS Nano 2021, 15, 10710−10721

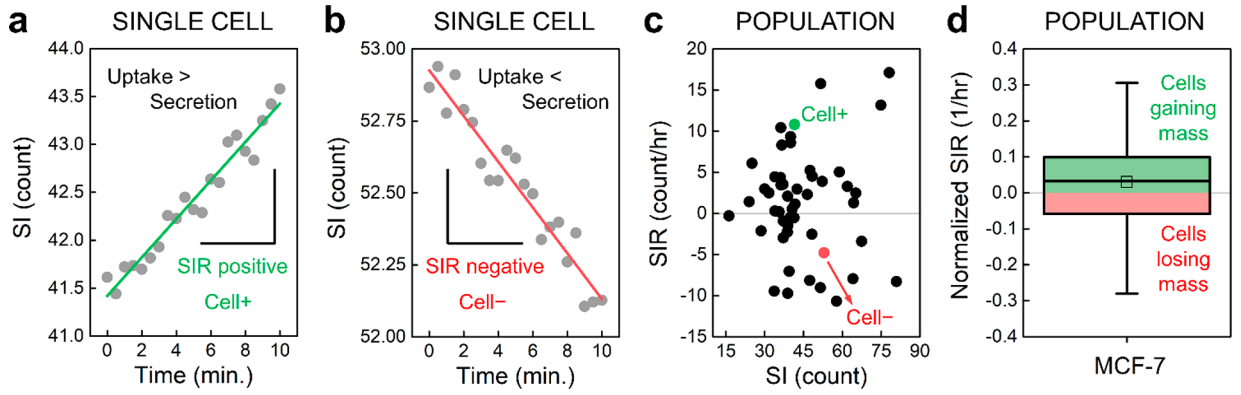

Figure 4. Plasmonic platform can assess heterogeneity in growth profile. The change in SI (gray dots) with time for a cell (a) gaining (green = positive SIR, uptake > secretion) and (b) losing (red = negative SIR, uptake < secretion) mass. (c) SIR *vs* SI data (SI at $t = 0$) for each cell (black dots), where the overall map shows the growth profile of the population. SIR values calculated for the cells in (a) and (b) are highlighted with green and red dots, respectively. (d) The same data in (c) is represented in a 1-dimensional box plot; *e.g.*, SIR was normalized by SI of each cell. The box plot represents the interquartile range, and the squares inside represent the average of the normalized SIR data. Number of MCF-7 cells used in each population measurement is 50.

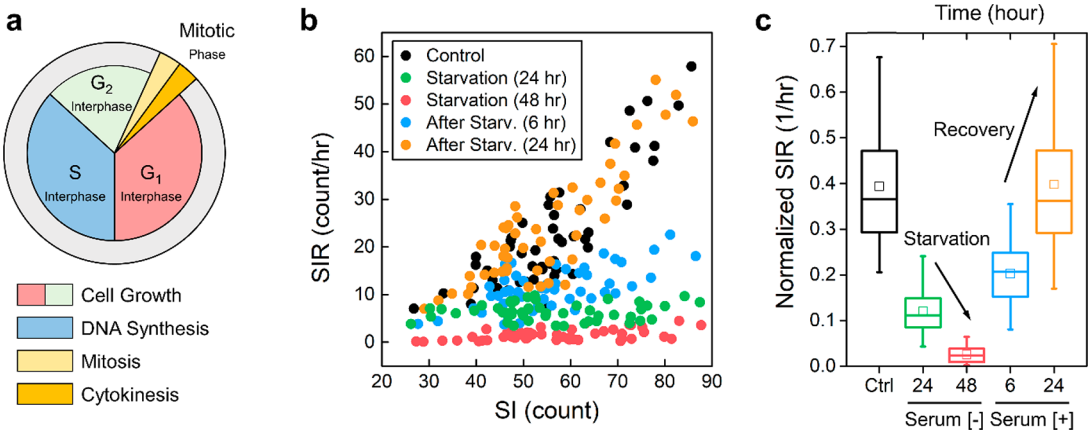

Figure 5. Antigrowth effect of starvation on MCF-7 cells. (a) Cell cycle consists of three interphases and mitotic phase. (b) SIR *vs* SI data of MCF-7 cells. (i) Reduction in cell growth due to starvation, *e.g.*, cells under complete medium (black) was transferred to serum-free medium (24/48 h starvation: green/red). (ii) Improvement in cell growth due to the addition of growth factors, *e.g.*, cells under serum-free medium for 48 h (red) was transferred to complete medium (6/24 h after starvation: blue/orange). (c) Variations within the normalized SIR profile during a 72 h period, where growth factors were added to the serum-free medium after 48 h to recover from arrest. Box plot represents the interquartile range, and the squares inside represent the average of the normalized SIR data. Number of MCF-7 cells used in each population measurement is 50.

I, cell−substrate contact locations are low in number and cell adhesion is weak, we incubated the cells on the surface of the plasmonic chip for 8 h prior to spectral measurements (gray area in the figure). This eliminates any spectral fluctuations due to detachments from the surface since the cells were initially in suspension due to trypsinization. As cells started to attach on the surface and the number of contact location increased (Phase II), we observed dramatic spectral shifts within the transmission resonance of the nanohole arrays. After ~18 h (highlighted with a dashed black line in the figure), we observed that the exponential behavior of the spectral variations switched to a linear one, since in Phase III, cells strongly adhered on the chip surface, and cell adhesion would no longer alter the transmission response. In this stage, two physical factors could alter the spectral variations, *e.g.*, mass accumulation or cell migration. Therefore, for one cell, spectral contributions due to migration was eliminated by CytoD, dosed at $t = 21$ h (green), while the other one remained in the normal cell medium (red). After dosing with CytoD for 10 h, we started to take measurements for the same cells (dashed lines for each curve corresponds to a 10 h long period with no data taken). In Figure 3c, we zoomed to a 2 h wide window, showing the spectral profiles for CytoD [+] and CytoD [−] cells. The similarity between spectral variations determined for two cells suggests that cell migration does not contribute to the spectral variations. The population study in Figure S2, where we compared the overall growth profile of 50 cells, also demonstrated such similarity between cells under CytoD and CytoD-free media. We also investigated the spectral variations for a formalin-fixed cell (blue); *e.g.*, no mass change or cell migration could exist. Here, the fluctuations in the spectral position of the transmission resonance are at the level of the spectral resolution of the spectrometer, which could be attributed only to instrumental noise.

Plasmonic Platform Determines Heterogeneity in Cell-Growth Profile. Parts a and b of Figure 4 show the real-time change in SI for two different cells over the course of 10 min. In the figures, positive SIR (green line) corresponds to a cell gaining mass and negative SIR (red line) corresponds to a cell losing mass. Mapping SIR *vs* SI data, where the *x*-axis is

https://doi.org/10.1021/acsnano.1c04031
ACS Nano 2021, 15, 10710−10721

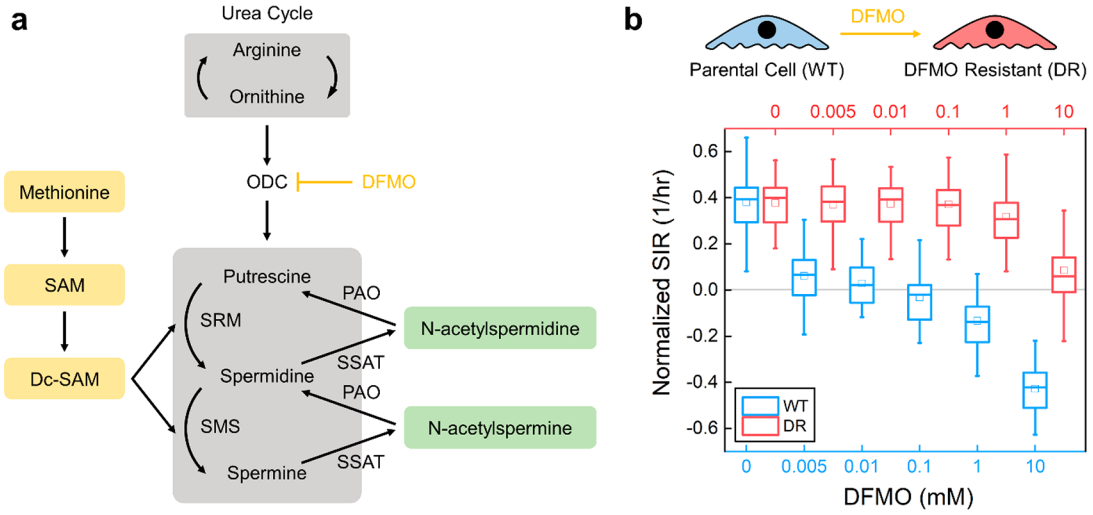

Figure 6. Antigrowth effect of DFMO on WT cells and the resistance of DR cells to DFMO's negative effect on cell growth. (a) Polyamine metabolism. Polyamine synthesis could be inhibited by an ODC inhibitor, DFMO. (b) Normalized SIR profile determined for WT (blue) and DR (red) MCF-7 cells under different DFMO concentrations. DR cells were derived from WT cells by gradually exposing WT cells to different DFMO concentrations. In the figure, box plot represents the interquartile range, and the squares inside represent the average of the normalized SIR data. Number of MCF-7 cells used in each population measurement is 50.

the initial SI value calculated for each cell (SI at t = 0), we generated the 2-dimensional growth profile of the population in single-cell level. In our platform, the 2-dimensional growth profile of cells (*e.g.*, mass accumulation rate *vs* mass) is represented by SIR *vs* SI data. Figure 4c shows the growth profile of an MCF-7 population, demonstrating the heterogeneity in mass (SI) and mass accumulation rate (SIR) across the population. Our platform could successfully identify cells with large or small masses and positive, zero, or negative mass accumulation rate. SIR *vs* SI data corresponding to the cells shown in Figure 4a ,b were denoted with green and red dots in Figure 4c. For single-cell measurements, we used a 100× objective lens which provides a 150 μm × 150 μm wide field of view that includes a cell adhered on the sensing surface and the cell medium covering the rest of the Al surface. Therefore, in order to eliminate the spectral contribution of the cell medium on SI calculation, we divided the SI value calculated for the sensor region of a single cell in the center by that of the control region consisting only cell medium. This eliminates any spectral variation due to background, which yields sensing data solely associated with accumulation or loss of cell mass. Furthermore, we separated each cell from one another by at least 150 μm by seeding cells on the plasmonic chip surface with low concentrations, *e.g.*, 1 × 10^4 cells/mL in order to eliminate interactions between cells and interference of data derived from different cells, which ensures growth profiles in single-cell precision. Figure 4d represents the same growth profile, where SIR was normalized by SI. Here, the reason to represent this 2-dimensional data on a single axis is to eliminate the size or cell cycle-dependent effects associated with the clonal cell lines, where the mass is characterized as a proxy for cell cycle position.[4,19] More importantly, in order to map a reliable growth profile, it is critical to remove any cellular behavior that could be distinct from the population. For example, for growth profile calculations, we excluded cells in doubling progress or cell clusters containing multiple cells (see Supporting Figure S3 for the comparison between single cells and a doubling cell).

Plasmonic Platform Determines the Effects of Serum Starvation on Cell Growth. In order to show the capability of our platform on determining intracellular pathways through *ex vivo* measurements, we first investigated the effect of starvation on cell growth. Figure 5a shows the cell cycle, which is the series of growth and development steps, starting with the formation of a new cell following a division and ending with the division of that cell to give rise to two daughter cells (see the Supporting Information for the details of cell cycle interphases). As shown in the literature, serum starvation results in a reversible cell cycle arrest at G1 phase, where cells require exogenous growth factors' stimuli to progress through the cell cycle. Cells can be released from the arrest and progress toward S/G2/M phases after introducing serum to the medium.[20] To maintain cell cultures, we used complete medium that contains RPMI 1640 to provide essential components such as amino acids, sugar, and salt and 10% fetal bovine serum (FBS), which provides the growth factors to stimulate cell growth. In this section, we investigated the effect of serum starvation on cell growth by monitoring cells in complete and serum-free medium. As stated in the previous section, spectral contributions due to cell medium were eliminated by normalizing the transmission response of the sensor region by that of control. When comparing cell responses under different media, refractive index differences add another spectral variation. For instance, transmission resonance of nanohole arrays under complete and serum-free media is located at ∼699 and ∼698 nm, respectively. Therefore, we positioned the integral window based on the initial location of the transmission resonance, *e.g.*, complete medium ∼727 and serum-free medium ∼726, while keeping its width constant at 60 nm. This eliminated any spectral variation due to cell media in the growth-profile calculations. Figure 5b shows SIR *vs* SI data of MCF-7 cells, demonstrating how their growth profile changes based on FBS. We could monitor the arrest response of cells by suspending growth factors. Compared to the control group (black: cells under complete medium), 24 h starvation, dramatically reduced the cell growth which could be clearly seen in the figure (green). Furthermore,

https://doi.org/10.1021/acsnano.1c04031
ACS Nano 2021, 15, 10710−10721

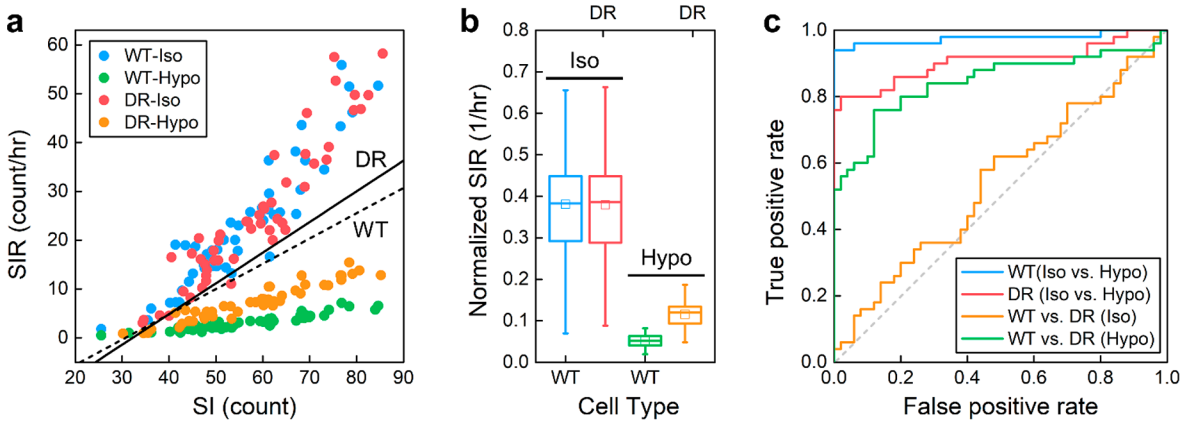

Figure 7. ODC-overproducing cells show higher growth rate in hypoosmotic stress. (a) SIR *vs* SI data for WT and DR cells in isosmotic (blue and red) and hypoosmotic (green and orange) media. In the figure, growth profiles determined for isosmotic and hypoosmotic (cell media + DI-water, 1:1) cases were separated by an overlay of an orthogonal vector, which designates the threshold obtained from LDA (solid line: DR, dashed line: WT). (b) Same data in 1-dimension, where SIR was normalized by SI of each cell. Box plots: WT: blue and green, DR: red and orange. (c) ROC curves for WT and DR cells, where each cell line was evaluated with itself under isosmotic *vs* hypoosmotic conditions (blue: WT and red: DR), and one another under isosmotic (orange) and hypoosmotic (green) conditions. In the figure, box plot represents the interquartile range, and the squares inside represent the average of the normalized SIR data. Number of MCF-7 cells used in each population measurement is 50.

SIR of most cells converged to zero under 48 h starvation (red). Providing growth factors with serum (serum-free to complete medium) triggers cell growth. For example, 6 h after introducing FBS to the medium, growth rate gradually increased (blue). After 24 h (orange), growth profile converged to that of the control group. Normalized SIR profile in Figure 5c also shows the cell cycle arrest within 48 h, while cells recovered their growth profile within 24 h by adding growth factors to the serum-free medium. For example, mean normalized SIR value for control, 0.3939 (black), decreased to 0.1200 and 0.0252 after 24 (green) and 48 h (red) stay in the serum-free medium. On the other hand, mean normalized SIR increased to 0.2024 and 0.3979 after 6 (blue) and 24 h (orange) upon the addition of FBS to the cell medium.

Plasmonic Platform Determines the Effect of an Intracellular Metabolism on Cell Growth. For further demonstration of our platform's ability to assess intracellular metabolism, we studied an important metabolism in cells that plays an important role in cell growth, polyamine metabolism.[21] Figure 6a shows the schematic illustration of polyamine metabolism (see the Supporting Information for the details of polyamine metabolism). In this metabolism, ornithine decarboxylase (ODC) is the enzyme required for the first stage in polyamine synthesis, and it is the key enzyme involved in its regulation.[22] High ODC activity increases polyamine synthesis in cancer cells; *i.e.*, direct inhibition of ODC activity could lead an antigrowth effect, *e.g.*, increasing apoptosis or decreasing tumor invasion.[23] In one path, polyamine synthesis could be inhibited by DFMO, which is an irreversible inhibitor of ODC.[24] Many clinical studies investigating different cancer types showed DFMO's antitumor effect *via* inhibiting polyamine synthesis.[25] Figure 6b shows the normalized SIR values for Wild Type (WT) MCF-7 cells under different DFMO concentrations (blue data), *e.g.*, 0−10 mM. Here, the cells were seeded in the media containing DFMO 6 h prior to the growth-profiling measurements. The antigrowth effect of DFMO on WT cells could be clearly seen from the decrease in their SIR profile.[23] For example, the mean normalized SIR value for control, 0.3811 (DFMO = 0), decreased to 0.0612 (DFMO = 0.05), 0.0282 (DFMO = 0.01), −0.0322 (DFMO = 0.1), −0.1336 (DFMO = 1), and −0.4280 (DFMO = 10). We also performed different statistical methods to reveal differences between growth profiles of populations. For example, we performed Welch's *t* test at α = 5% significance level (where α is between 0 and 1); *i.e.*, no significant difference could be detected if $p > 0.05$. Normalized SIR data of the population under different DFMO concentrations were compared with that of control, where *p*-values were Bonferroni corrected. The further decrease in SIR profile with DFMO concentration could be also seen with *p*-values, *e.g.*, p(control *vs* DFMO = 0.005, 0.01, 0.1, 1, 10) = 4.6380×10^{-25}, 2.8621×10^{-28}, 4.9378×10^{-32}, 4.2553×10^{-36}, and 2.6921×10^{-51}.

As shown in the literature, ODC activity is amplified, and cells overproduce ODC upon exposure to DFMO for long periods of time.[26] In order to demonstrate this fact, we prepared a DFMO-Resistant (DR) cell line as an adherent culture by gradually exposing MCF-7 cells to different DFMO concentrations as described previously.[27] (see the Methods for the preparation of the DR cell line). Figure 6b (red data) shows the strong resistance of DR cells to DMFO's negative effect on cell growth. Cell growth remains unchanged until DFMO = 1 mM; *e.g.*, mean normalized SIR values are 0.3780 (control, DFMO = 0), 0.3712 (DFMO = 0.05), 0.3740 (DFMO = 0.01), 0.3714 (DFMO = 0.1), 0.3175 (DFMO = 1), and 0.0855 (DFMO = 10). This resistant behavior could be also seen with Welch's *t* test, *e.g.*, *p*(control *vs* DFMO = 0.005, 0.01, 0.1, 1, 10) = 0.7792, 0.7985, 0.7812, 0.0250, and 5.0050×10^{-18}. Such resistant behavior to the negative effect of DFMO on cell growth is directly related to the higher ODC activity of DR cells compared to WT cells as shown earlier in literature.[28] These results demonstrate the ability of our platform to differentiate biophysical differences between cells. Here, DFMO was diluted with dimethyl sulfoxide (DMSO), which does not alter the growth profile as shown in Supporting Figure S2. More importantly, DFMO is a targeted therapeutic agent thanks to its ability to inhibit ODC activity, which has been used for a variety of cancer types.[29] Hence, this result also demonstrates our platform's ability to assess therapeutic

https://doi.org/10.1021/acsnano.1c04031
ACS Nano 2021, 15, 10710−10721

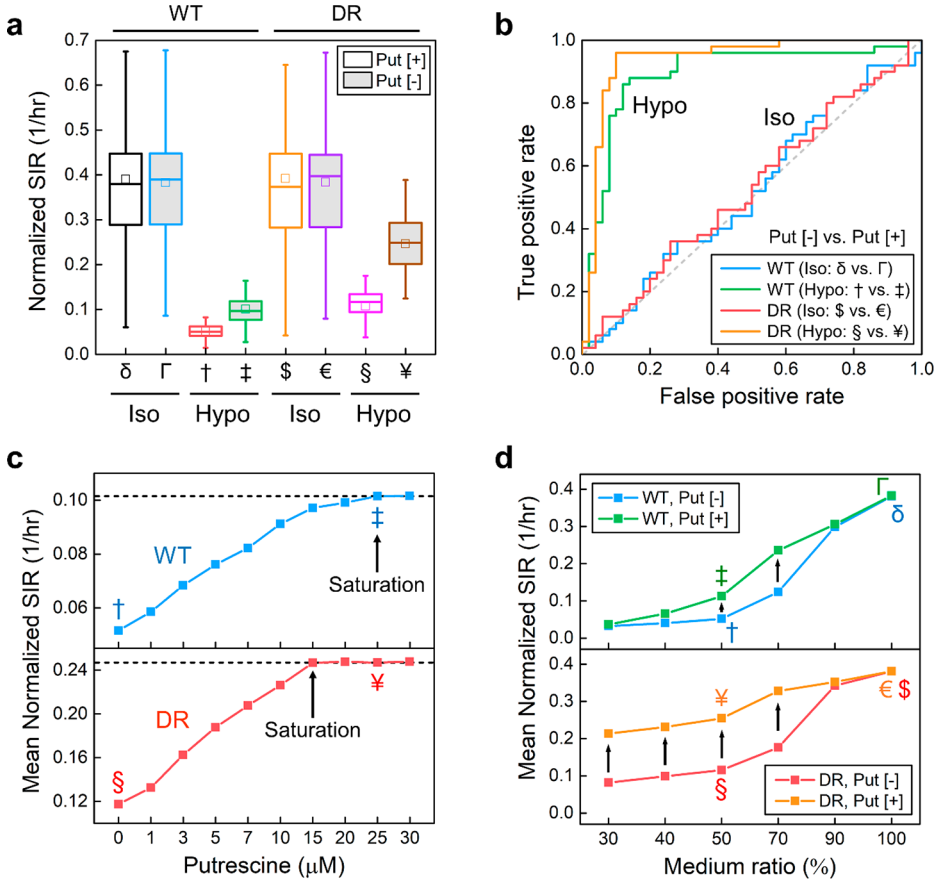

Figure 8. Effect of exogenous putrescine on cell-growth profile. (a) Normalized SIR profile for WT and DR cells under isosmotic and hypoosmotic (cell media + DI-water, 1:1) cell media without (WT: black, red and DR: orange, magenta) and with exogenous putrescine (WT: blue, green and DR: violet, brown). In the figure, box plots represent the interquartile range and squares inside represent the average of the normalized SIR data. (b) ROC curves for WT and DR cells under isosmotic and hypoosmotic cell media without and with exogenous putrescine. Each cell line is evaluated with itself under different osmolarity conditions in the presence and absence of putrescine. Isosmotic media; Put [−] *vs* Put [+], blue: WT and red: DR. Hypoosmotic media; Put [−] *vs* Put [+], green: WT and orange: DR. (c) Mean normalized SIR values calculated for WT (blue) and DR (red) cells under a hypoosmotic media (cell media + DI-water, 1:1) with different exogenous putrescine concentrations. Putrescine concentrations for saturation condition are denoted with arrows for both cell lines. (d) Mean normalized SIR values calculated for WT (blue, green: Put [−], Put [+]) and DR (red, orange: Put [−], Put [+]) cells under the solution (cell media + DI-water) with different medium ratio. Arrows indicate the increase in growth rate due to the addition of putrescine. Number of MCF-7 cells used in each population measurement is 50.

response of cancer models *via* monitoring their growth profile under certain drug therapies. In the future, we will evaluate our platform from this aspect by studying therapeutic effects of well-known standard-of-care drugs; *e.g.*, a stable or decreasing SIR profile in response to drug treatment could be related to therapeutic resistance or susceptibility.

Plasmonic Platform Determines Polyamine Metabolism under Hypoosmotic Stress. Using our cell-growth profiling platform, we could indirectly evaluate ODC activity of MCF-7 cells under an external stimulus. As demonstrated with the use of bulk functional assays based on cell cultures in literature, cells show dramatic reduction in their growth profile upon a long-term hypoosmotic shock.[28] Using our functional assay platform, we could demonstrate this cellular behavior over a much shorter time and in single-cell precision. We investigated the effect of osmotic stress on ODC activity by monitoring mass accumulation in real-time for MCF-7 cells under low osmolarity; *e.g.*, the hypoosmotic media is composed of normal cell medium and deionized (DI)-water with 1:1 ratio.

Figure 7a shows SIR *vs* SI data for WT and DR cells under isosmotic and hypoosmotic conditions. As previously shown, sudden interchanges between isosmotic and hypoosmotic conditions do not vary mass accumulation rate.[30] Therefore, we exposed cells to hypoosmotic media 8 h prior to each test. As stated in the previous section, refractive index differences arising from media with different osmolarity add another spectral variation. Transmission resonance of nanohole arrays under isosmotic and hypoosmotic cell media is located at ∼699 and ∼695 nm, respectively. Therefore, we positioned the integral window at ∼727 (isosmotic) and ∼723 (hypoosmotic), while keeping its width constant at 60 nm. In addition to normalizing transmission response of sensor by control, modifying position of the spectral window eliminated the spectral variations due to cell media. As shown in Figure 7a, the similarity between growth profiles for WT and DR cells under isosmotic condition (blue *vs* red dots) could be no longer observed upon the decrease in osmolarity (green *vs* orange).[31] Moreover, as shown in the literature, the decrease in growth rate is more pronounced for WT cells compared to DR cells.[31] Figure 7b shows the normalized SIR profile for WT

https://doi.org/10.1021/acsnano.1c04031
ACS Nano 2021, 15, 10710−10721

(blue and green) and DR (red and orange) cells under isosmotic and hypoosmotic conditions. Here, the similarity between growth profiles under isosmotic media could be seen in mean normalized SIR, *e.g.*, 0.3805 (WT) and 0.3794 (DR). Welch's *t* test also confirms this similarity, *e.g.*, p(WT *vs* DR under isosmotic) = 0.9702. On the other hand, under low osmolarity, while both cell lines show a dramatic reduction in their growth profile, DR cells have a higher growth rate compared to WT cells; *e.g.*, mean normalized SIR is 0.0516 (WT) and 0.1151 (DR). The larger reduction in growth rate for WT cells could be also observed with Welch's *t* test, where WT cells under isosmotic and hypoosmotic conditions are more separated from one another, *e.g.*, p(WT under isosmotic *vs* hypoosmotic) = 1.8401×10^{-30} and (DR under isosmotic *vs* hypoosmotic) = 2.2629×10^{-21}. The dissimilarity between growth profiles of WT and DR cells in the hypoosmotic case could be seen with p(WT *vs* DR under hypoosmotic) = 1.2435×10^{-17}. These results demonstrate DR cells' advantage over WT cells to proliferate at low osmolarity, which is directly attributed to the high ODC activity for DR cells.[28,31]

In order to demonstrate the quality of our cell-growth profiling platform in assessing intracellular pathways and classifying cells based on their cellular response, we determined receiver-operating characteristics (ROC) after performing linear discriminate analysis (LDA) on MCF-7 cells under different conditions. Using LDA, we projected the 2-dimensional SIR *vs* SI data onto a single axis, which differentiates two cell groups best and defines a threshold for their classification. In Figure 7a, the solid black line separates the growth profile of DR cells under isosmotic (red) and hypoosmotic media (orange), while the dashed black line separates the growth profile of WT cells under isosmotic (blue) and hypoosmotic media (green). Considering the fact that WT and DR cells possess similar growth profiles under isosmotic media, the smaller slope of the LDA curve for WT cells compared to DR cells proves the higher distinction between WT cells under isosmotic and hypoosmotic conditions, which is attributed to the larger loss in growth rate for WT cells. Performing ROC curve analysis and calculating the area under the curve (AUC), we provided a metric to identify each cell's classification as sensitive or resistant to the external factors,[16] where random and perfect classifiers have AUC = 0.5 and 1, respectively. Figure 7c shows the ROC curves for WT and DR cells under different scenarios. For isosmotic conditions, WT and DR cells are indistinguishable from one another, *e.g.*, AUC(WT *vs* DR under isosmotic) = 0.5438 (orange line). On the other hand, under hypoosmotic condition, ROC analysis shows an excellent resolution of WT and DR cells, *e.g.*, AUC(WT *vs* DR under hypoosmotic) = 0.8444 (green line). This is due to higher ODC activity for DR cells that separates its growth profile from that of WT cells. The distinction between growth profiles under low osmolarity could be also revealed by comparing growth profile of each cell line before and after the osmotic shock, *e.g.*, AUC(WT under isosmotic *vs* hypoosmotic) = 0.9764 (blue line), and AUC(DR under isosmotic *vs* hypoosmotic) = 0.9060 (red line). Here, higher AUC for WT cells is due to larger separation from the growth profile of isosmotic condition by the hypoosmotic stress.

Uptake of Exogenous Polyamines Recovers ODC Inhibition. As stated previously, polyamines are the key players in cell growth, and the three polyamines, *e.g.*, putrescine, spermidine and spermine, are regulated by ODC,[32] catalyzing the synthesis of putrescine. Therefore, polyamine synthesis is strongly effected by sudden hypoosmotic shock.[33] As shown in literature utilizing long-term cell cultures, ODC inhibition due to low osmolarity could be rescued by exogenous putrescine.[31] Adding putrescine to a hypoosmotic medium, ODC-overproducing cells accumulate more putrescine, which could dramatically improve their growth compared to their parental counterparts. Figure 8a shows the normalized SIR profile for WT and DR cells under isosmotic and hypoosmotic media without and with 25 μM putrescine. Under isosmotic conditions, putrescine does not alter the growth profile for WT and DR cells.[31] This fact could be seen in SIR profiles, *e.g.*, Figure 8a: WT(without and with putrescine) are denoted with δ and Γ, and DR(without and with putrescine) are denoted with \$ and €. For WT cells under isotropic conditions, mean normalized SIR values were calculated as 0.3827 (δ = black line) and 0.3904 (Γ = blue line). Similarly for DR cells, mean normalized SIR values were calculated as 0.3839 (\$ = orange) and 0.3919 (€ = violet). ROC analysis (Figure 8b) also shows this similarity in growth profile under isosmotic conditions, *e.g.*, for WT cells AUC(blue curve: Put [−] *vs* Put [+]) = 0.520, and for DR cells AUC(red curve: Put [−] *vs* Put [+]) = 0.526. Unlike the isosmotic case, exogenous putrescine improves cell growth (which is degraded by low osmolarity) for both cell lines under hypoosmotic shock.[31] Here, the increase in mean normalized SIR is much higher for DR cells compared to WT cells. In Figure 8a, WT(without and with putrescine) are denoted with † and ‡ and DR(without and with putrescine) are denoted with § and ¥. The presence of putrescine increased mean normalized SIR from 0.0516 († = red) to 0.1010 (‡ = green) for WT cells and from 0.1075 (§ = magenta) to 0.2467 (¥ = brown) for DR cells. This better improvement in growth rate for DR cells could be also seen *via* ROC analysis in Figure 8b, *e.g.*, for WT cells AUC(green curve: Put [−] *vs* Put [+]) = 0.892, and for DR cells AUC(orange curve: Put [−] *vs* Put [+]) = 0.9384, demonstrating a larger difference in growth profile for DR cells after adding putrescine to the hypoosmotic media.

Requiring more putrescine to maintain cell growth under hypoosmotic shock makes cells more dependent on exogenous putrescine compared to their ODC-overproducing variants.[31] This fact could be seen from mean normalized SIR values calculated for different putrescine concentrations (Figure 8c). For each measurement, cells were exposed to the corresponding medium 8 h prior to the test. In the figure, the symbols † and ‡ (blue: WT cells) and § and ¥ (red: DR cells) correspond to the mean of the normalized SIR data shown in Figure 8a. Under hypoosmotic medium (cell medium + DI-water, 1:1), putrescine concentration to saturate mean normalized SIR for WT cells (25 μM) is larger than DR cells (15 μM), which demonstrates WT cells' higher dependence on putrescine to proliferate under hypoosmotic shock. Moreover in low osmolarity, WT cells exhibit lower growth rate compared to DR cells for every putrescine condition.

As shown in the literature based on long-term and high-volume cell cultures, DR cells have better adaptation to hypoosmotic conditions due to their high ODC activity and intracellular putrescine content.[31] Figure 8d shows the mean normalized SIR values calculated for different medium ratio (percentage ratio of medium/medium + DI-water), where the cells were exposed to the corresponding medium 8 h prior to each test. In the figure, the symbols, δ, Γ, †, ‡, \$, €, §, and ¥ correspond to the mean of the normalized SIR data shown in Figure 8a. WT cells showed a poor growth profile under

https://doi.org/10.1021/acsnano.1c04031
ACS Nano 2021, 15, 10710−10721

hypoosmotic shock (blue and green: Put [−] and Put [+]), and needed more putrescine to show similar improvements in growth rate observed in DR cells (red and orange: Put [−] and Put [+]). Up to 50% medium ratio, improvement in growth profile by exogenous putrescine is low, which demonstrates WT cells' sensitivity to putrescine for survival under very low osmolarity. Between 50% and 90%, improvement in growth profile is mostly attributed to the increase in osmolarity, which decreases the dependence toward putrescine for proliferation, *i.e.*, for this range, larger improvements were observed in the mean normalized SIR with putrescine (highlighted with arrows from blue to green curve). On the other hand, for DR cells, we observed a consistent improvement in the growth rate with medium ratio in the presence of putrescine (highlighted with arrows from red to orange curve). Much faster recovery of growth rate under lower medium ratio proves DR cells' ability to survive in very low osmolarity, which is directly related to their higher ODC activity. This high ODC activity helps DR cells to improve their growth profile after the addition of putrescine to the cell medium.[31]

Cells with High ODC Activity Recover Faster after Hypoosmotic Shock. Thanks to their high ODC activity, DR cells could adapt to hypoosmotic shock, and when reversing to isosmotic conditions, they could recover their growth profile much faster compared to WT cells.[31] Figure S4 shows the mean normalized SIR values calculated for WT (blue) and DR (red) cells at different times after transferring them from isosmotic to hypoosmotic media. Here, the growth rate of DR cells increases much faster with time compared to WT cells, demonstrating their better adaptation to new osmolarity conditions. Accordingly, DR cells need much shorter time to recover back to the original growth profile (denoted with dashed arrows) compared to WT cells, *e.g.*, 48 and 64 h for DR and WT cells, respectively.

CONCLUSIONS

In this paper, we demonstrated a label-free and plasmonic functional assay platform that can determine growth profiles of cells in real-time. The platform could serve in variety of *ex vivo* applications without the need for high-volume cell cultures, *e.g.*, investigating biophysical properties of cells, determining intracellular pathways, and monitoring dynamic cell activities. Accessing cell responses to particular drug treatments could provide vital information on drug resistance, and allow characterization of phenotypic subpopulations. Determining heterogeneity in growth profile could provide information on the effects of cell cycle dependent pathways and dynamics of different cell metabolisms.

Bringing a modality into the literature, our functional assay platform could enable *ex vivo* analyses in basic and clinical research. Despite its strong growth-profiling capability, our platform demands further optimization to bring more modalities required for practicality. (i) The current technique is compatible with adherent cell models since it is based on sensing the accumulated mass on the plasmonic surface. The reliability of the platform depends on the complete attachment of cells, which ensures elimination of spectral variations due to detachment of cells from the surface. In order to adapt our platform for suspended cells, bounding agents could be utilized on the plasmonic surface, *e.g.*, poly-L-lysine (PLL), which is a well-known polymer acting as an electrostatic force to attach cells without chemical modification of the cell membrane, and ensure immobilization without affecting the cell physiology.[34] (ii) Plasmonic substrates with much sharper optical responses could provide stronger spectral variations in the presence of low refractive index changes. This could provide sensing signals corresponding to mass change of single cells within much shorter time, which could shorten the measurement duration to increase the throughput for population studies. (iii) In the current version, we manually picked the position of the integral window. This position could be automatically determined based on the parameters providing the most reliable and sensitive information. This feature could strengthen the practicality of our platform, and provide a user-friendly software infrastructure. (iv) The platform provides low throughput since each single-cell measurement lasts 10 min. Throughput could be improved by performing growth-profiling measurements simultaneously, where the sensor locations on the plasmonic chip surface are evaluated all at the same time. By integrating a narrow bandwidth light source, *e.g.*, an LED or a laser, and an imaging device, *e.g.*, a CMOS or a CCD camera, we could determine spectral variations by monitoring intensity changes within diffraction field images as shown previously.[35] By using a camera, we could also eliminate migrating or doubling cells in growth-profiling calculations.

These improvements could ensure a plasmonic functional assay platform that could allow single cell analyses to assess population heterogeneity in short durations for faster test results. The technique could be also applicable to any scenario, where cell mass is affected ranging from tumorigenic growth to metabolic disorders. The platform will be also able to provide therapeutic profile of cancer patients for wide range of standard-of-care drugs, which will help doctors to determine personalized drug therapies.

METHODS

Plasmonic Chip. Figure 1a shows the schematic illustration of the plasmonic chip employing nanohole arrays fabricated through a 120 nm thick aluminum (Al) film. The top metal surface was coated with a 2 nm thick silicon dioxide (SiO_2) layer, which prevents oxidation of the film. This layer also stimulates cell adhesion on the sensing surface compared to the metal film itself. Since the tail of the evanescent fields (vertically positioned to the sensing surface) is much longer compared to the thickness of the SiO_2 layer, this thin layer does not affect light–matter interaction on the sensing surface.[36] The Al film stands on a 100 nm thick silicon nitride (SiN) interlayer coated on a fused silica substrate (glass). SiN interlayer was used as a high reactive index material to eliminate plasmonic modes excited between Al and glass, which result in unwanted spectral features within the visible spectrum due to the low refractive index of fused silica. Thanks to this approach, we could create a well-defined and isolated plasmonic mode within the spectral window of interest as discussed earlier.[37]

Experimental Setup. A broadband white light-emitting diode (LED) source was used to illuminate the plasmonic chip. The light transmitted from the plasmonic chip was collected by a 100× objective lens in a Zeiss Axio Observer 7 inverted microscope. The collected light was fiber-coupled to an AvaSpec Multichannel Spectrometer with a light-coupling scheme, including an achromatic and an objective lens, and a fiber collimator. In the multichannel spectrometer, the spectral range of interest was divided with five simultaneously working spectrometers, and a 5 μm slit width was used to achieve a spectral resolution as high as 0.9 Å. This value was provided by Avantes BV based on actual statistics rather than theoretical calculations. Considering such small mass changes, *e.g.*, in sub-1 picogram/hour levels,[4] mechanical effects on the optical readout was eliminated with a vibration isolator. We also utilized a motorized translation stage in the fiber-coupling mechanism to precisely couple light transmitted from plasmonic chips to the fiber.

https://doi.org/10.1021/acsnano.1c04031
ACS Nano 2021, 15, 10710−10721

For a reliable mass calculation from the experimental data, transmission response of the nanohole arrays was smoothen with Savitzky–Golay filter. In order to maintain cell cultures during growth profiling measurements, we used a PeCon cell culture incubator and a Zeiss incubation control platform, *e.g.*, CO_2 level of 5%, temperature of 37.0 °C and humidity level of 95%.

Cell Culture Preparation. MCF-7 cells (ATCC HTB-22) were regularly maintained in RPMI 1640 medium supplemented with 10% FBS, 10% penicillin, and 1% nonessential amino acids. The cells were incubated in a humidified Thermo Scientific Forma 371 incubator at 37 °C and with 5% CO_2.

Fabrication of the Plasmonic Chips. We performed the fabrication process on a 4 in. fused silica wafer coated with 100 nm LPCVD (low pressure chemical vapor deposition) SiN layer on top. We first coated the SiN surface with 5 nm titanium (adhesion layer) and 120 nm Al. We then coated the Al surface with a photoresist and performed deep-ultraviolet lithography *via* a mask to define periodic nanoholes throughout the surface. After the development of photoresist, we etched the Al film with ion-beam milling to realize nanohole arrays. We removed the remaining photoresist from the surface with oxygen plasma cleaning, and the Al surface was coated with 2 nm SiO_2. This SiO_2 layer helps to maintain the plasmonic properties, which could be effected by the degradation of surface due to the oxidation of aluminum (see Supporting Figure S5 for the analyses of plasmonic chips). Finally, we diced the wafer to realize 2 cm × 1 cm plasmonic chips. This wafer-scale fabrication technique provides high-throughput without sacrificing from quality, and enables the realization of nanoholes faster and cheaper compared to the classical methods based on electron-beam lithography.[38]

Chip Preparation for Cell Seeding. Surface of the plasmonic chips was coated with a polymer to protect the chip surface during the dicing step. This polymer layer was removed with piranha solution which is composed of 3:1, sulfuric acid: hydrogen peroxide, and rinsed with DI-water. Plasmonic chip surface is silicon dioxide, which is inherently hydrophilic, *i.e.*, piranha cleaning leaves the surface more hydrophilic and prepares the surface for cell seeding. For growth-profiling experiments, 1×10^4 cells/mL were seeded on the chip surface 24 h prior to the measurements.

Preparation of DR Cell Line. MCF-7 cells were cultured in DFMO with stepwise increasing concentrations as following: 0, 0.05, 0.01, 0.1, 1, and 10 mM. Cells were treated with each concentration of DFMO for over 4 weeks before switching to the next concentration. The resistant cells were obtained within a period of 28 weeks. For each concentration, growth profile of DR culture was ensured to be comparable with that of WT cells. DR cells were maintained in the same media with WT cells with an addition of 0.1 mM DFMO every other passage.

ASSOCIATED CONTENT

Supporting Information

The Supporting Information is available free of charge at https://pubs.acs.org/doi/10.1021/acsnano.1c04031.

Transmission response of nanohole arrays embedded in cell media, cell adhesion phases, effects of DMSO and cell migration on growth profile of cells, growth measurements and microscope images of cells in mitosis and different masses, cell cycle interphases, polyamine metabolism, recovery of growth-profile of cells after hypoosmotic shock, and the function of the SiO_2 layer in the plasmonic chips (PDF)

AUTHOR INFORMATION

Corresponding Author

Arif E. Cetin − *Izmir Biomedicine and Genome Center, Balcova, Izmir 35340, Turkey;* orcid.org/0000-0002-0788-8108; Email: arifengin.cetin@ibg.edu.tr

Authors

Seda Nur Topkaya − *Department of Analytical Chemistry, Faculty of Pharmacy, Izmir Katip Celebi University, Cigli, Izmir 35620, Turkey*

Ozden Yalcin-Ozuysal − *Department of Molecular Biology and Genetics, Izmir Institute of Technology, Urla, Izmir 35430, Turkey*

Ali Khademhosseini − *Terasaki Institute for Biomedical Innovation, Los Angeles, California 90024, United States;* orcid.org/0000-0002-2692-1524

Complete contact information is available at: https://pubs.acs.org/10.1021/acsnano.1c04031

Author Contributions

A.E.C. conceived the idea and directed the project. A.E.C constructed the optical read-out setup. A.E.C. performed cell culturing and the corresponding osmolarity tests. A.E.C., S.N.T., O.Y.O., and A.K. designed and performed the growth-profiling experiments and analyzed the results. A.E.C., S.N.T., O.Y.O., and A.K. discussed and interpreted the data. A.E.C., S.N.T., O.Y.O., and A.K. wrote the manuscript.

Notes

The authors declare the following competing financial interest(s): A.E.C. has a pending patent application for the presented growth-profiling platform.

ACKNOWLEDGMENTS

A.E.C. acknowledges The Scientific and Technological Research Council of Turkey (TUBITAK) 3501 - Career Development Program (Project No. 119E111) and BAGEP Award of the Science Academy, Turkey. We thank Alper Bagriyanik and Nevin Ersoy for SEM imaging of the plasmonic chips and MCF-7 cells. We also thank Buket Onder for the illustrations.

REFERENCES

(1) Housman, G.; Byler, S.; Heerboth, S.; Lapinska, K.; Longacre, M.; Snyder, N.; Sarkar, S. Drug Resistance in Cancer: An Overview. *Cancers* **2014**, *6* (3), 1769–1792.

(2) Ferrezuelo, F.; Colomina, N.; Palmisano, A.; Gari, E.; Gallego, C.; Csikasz-Nagy, A.; Aldea, M. The Critical Size Is Set at a Single-Cell Level by Growth Rate to Attain Homeostasis and Adaptation. *Nat. Commun.* **2012**, *3* (1), 1012.

(3) Zangle, T. A.; Teitell, M. A. Live-Cell Mass Profiling: An Emerging Approach in Quantitative Biophysics. *Nat. Methods* **2014**, *11* (12), 1221–1228.

(4) Stevens, M. M.; Maire, C. L.; Chou, N.; Murakami, M. A.; Knoff, D. S.; Kikuchi, Y.; Kimmerling, R. J.; Liu, H.; Haidar, S.; Calistri, N. L.; Cermak, N.; Olcum, S.; Cordero, N. A.; Idbaih, A.; Wen, P. Y.; Weinstock, D. M.; Ligon, K. L.; Manalis, S. R. Drug Sensitivity of Single Cancer Cells Is Predicted by Changes in Mass Accumulation Rate. *Nat. Biotechnol.* **2016**, *34* (11), 1161–1167.

(5) Ambrosetti, E.; Paoletti, P.; Bosco, A.; Parisse, P.; Scaini, D.; Tagliabue, E.; de Marco, A.; Casalis, L. Quantification of Circulating Cancer Biomarkers *via* Sensitive Topographic Measurements on Single Binder Nanoarrays. *ACS Omega* **2017**, *2* (6), 2618–2629.

(6) Wang, Y.; Knoll, W.; Dostalek, J. Bacterial Pathogen Surface Plasmon Resonance Biosensor Advanced by Long Range Surface Plasmons and Magnetic Nanoparticle Assays. *Anal. Chem.* **2012**, *84* (19), 8345–8350.

(7) Lee, J.; Takemura, K.; Park, E. Plasmonic Nanomaterial-Based Optical Biosensing Platforms for Virus Detection. *Sensors* **2017**, *17* (10), 2332.

(8) Eletxigerra, U.; Martinez-Perdiguero, J.; Barderas, R.; Pingarrón, J. M.; Campuzano, S.; Merino, S. Surface Plasmon Resonance

Immunosensor for ErbB2 Breast Cancer Biomarker Determination in Human Serum and Raw Cancer Cell Lysates. *Anal. Chim. Acta* **2016**, *905*, 156−162.
(9) Giner-Casares, J. J.; Henriksen-Lacey, M.; Garcia, I.; Liz-Marzμn, L. M. Plasmonic Surfaces for Cell Growth and Retrieval Triggered by Near- Infrared Light. *Angew. Chem., Int. Ed.* **2016**, *55*, 974−978.
(10) Tu, L.; Li, X.; Bian, S.; Yu, Y.; Li, J.; Huang, L.; Liu, P. Label-Free and Real-Time Monitoring of Single Cell Attachment on Holes. *Sci. Rep.* **2017**, *7*, 1−11.
(11) Zhang, F.; Wang, S.; Yin, L.; Yang, Y.; Guan, Y.; Wang, W.; Xu, H.; Tao, N. Quantification of Epidermal Growth Factor Receptor Expression Level and Binding Kinetics on Cell Surfaces by Surface Plasmon Resonance Imaging. *Anal. Chem.* **2015**, *87* (19), 9960−9965.
(12) Li, X.; Soler, M.; Ozdemir, C. I.; Belushkin, A.; Yesilkoy, F.; Altug, H. Plasmonic Nanohole Array Biosensor for Label-Free and Real-Time Analysis of Live Cell Secretion. *Lab Chip* **2017**, *17* (13), 2208−2217.
(13) Li, X.; Soler, M.; Szydzik, C.; Khoshmanesh, K.; Schmidt, J.; Coukos, G.; Mitchell, A.; Altug, H. Label-Free Optofluidic Nanobiosensor Enables Real-Time Analysis of Single-Cell Cytokine Secretion. *Small* **2018**, *14* (26), 1800698.
(14) Cetin, A. E.; Yanik, A. A.; Yilmaz, C.; Somu, S.; Busnaina, A.; Altug, H. Monopole Antenna Arrays for Optical Trapping, Spectroscopy, and Sensing. *Appl. Phys. Lett.* **2011**, *98* (11), 111110.
(15) Cetin, A. E.; Topkaya, S. N. Photonic Crystal and Plasmonic Nanohole Based Label-Free Biodetection. *Biosens. Bioelectron.* **2019**, *132*, 196−202.
(16) Cetin, A. E.; Stevens, M. M.; Calistri, N. L.; Fulciniti, M.; Olcum, S.; Kimmerling, R. J.; Munshi, N. C.; Manalis, S. R. Determining Therapeutic Susceptibility in Multiple Myeloma by Single-Cell Mass Accumulation. *Nat. Commun.* **2017**, *8* (1), 1613.
(17) Yanik, A. A.; Cetin, A. E.; Huang, M.; Artar, A.; Mousavi, S. H.; Khanikaev, A.; Connor, J. H.; Shvets, G.; Altug, H. Seeing Protein Monolayers with Naked Eye through Plasmonic Fano Resonances. *Proc. Natl. Acad. Sci. U. S. A.* **2011**, *108* (29), 11784−11789.
(18) Hayot, C.; Debeir, O.; Van Ham, P.; Van Damme, M.; Kiss, R.; Decaestecker, C. Characterization of the Activities of Actin-Affecting Drugs on Tumor Cell Migration. *Toxicol. Appl. Pharmacol.* **2006**, *211* (1), 30−40.
(19) Son, S.; Tzur, A.; Weng, Y.; Jorgensen, P.; Kim, J.; Kirschner, M. W.; Manalis, S. R. Direct Observation of Mammalian Cell Growth and Size Regulation. *Nat. Methods* **2012**, *9* (9), 910−912.
(20) Piletz, J. E.; Drivon, J.; Eisenga, J.; Buck, W.; Yen, S.; McLin, M.; Meruvia, W.; Amaral, C.; Brue, K. Human Cells Grown With or Without Substitutes for Fetal Bovine Serum. *Cell Med.* **2018**, *10*, No. 215517901875514.
(21) Casero, R. A.; Pegg, A. E. Polyamine Catabolism and Disease. *Biochem. J.* **2009**, *421*, 323−338.
(22) Canizares, F.; Salinas, J.; De Las Heras, M.; Diaz, J.; Tovar, I.; Martinez, P.; Penafiel, R. Prognostic Value of Ornithine Decarboxylase and Polyamines in Human Breast Cancer: Correlation with Clinicopathologic Parameters. *Clin. Cancer Res.* **1999**, *5* (8), 2035−2041.
(23) Kremmer, T.; Palyi, I.; Daubner, D.; Boldizsar, M.; Vincze, B.; Paulik, E.; Sugar, J.; Pokorny, E.; Tury, E. Comparative Studies on the Polyamine Metabolism and DFMO Treatment of MCF-7 and MDA-MB-231 Breast Cancer Cell Lines and Xenografts. *Anticancer Res.* **1991**, *11* (5), 1807−1813.
(24) McCann, P. P.; Pegg, A. E. Ornithine Decarboxylase as an Enzyme Target for Therapy. *Pharmacol. Ther.* **1992**, *54* (2), 195−215.
(25) Alexiou, G. A.; Lianos, G. D.; Ragos, V.; Galani, V.; Kyritsis, A. P. Difluoromethylornithine in Cancer: New Advances. *Future Oncol.* **2017**, *13* (9), 809.
(26) Pegg, A. E.; Secrist, J. A.; Madhubala, R. Properties of L1210 Cells Resistant to α-Difluoromethylornithine. *Cancer Res.* **1988**, *48*, 2678−2682.
(27) Das, B.; Vig, M.; Khurana, K. K.; Madhubala, R. Isolation and Characterization of Human Breast Adenocarcinoma Cells Made Resistant to α-Difluoromethylornithine. *Cancer Invest.* **2000**, *18* (2), 115−122.
(28) Poulin, R.; Pegg, A. E. Regulation of Ornithine Decarboxylase Expression by Anisosmotic Shock in α-Difluoromethylornithine-Resistant L1210 Cells. *J. Biol. Chem.* **1990**, *265* (7), 4025−4032.
(29) Sholler, G. L. S.; Ferguson, W.; Bergendahl, G.; Bond, J. P.; Neville, K.; Eslin, D.; Brown, V.; Roberts, W.; Wada, R. K.; Oesterheld, J.; Mitchell, D.; Foley, J.; Parikh, N. S.; Eshun, F.; Zage, P.; Rawwas, J.; Sencer, S.; Pankiewicz, D.; Quinn, M.; Rich, M.; Junewick, J.; Kraveka, J. M. Maintenance DFMO Increases Survival in High Risk Neuroblastoma. *Sci. Rep.* **2018**, *8* (14445), 1−9.
(30) Son, S.; Stevens, M. M.; Chao, H. X.; Thoreen, C.; Hosios, A. M.; Schweitzer, L. D.; Weng, Y.; Wood, K.; Sabatini, D.; Vander Heiden, M. G.; Manalis, S. Cooperative Nutrient Accumulation Sustains Growth of Mammalian Cells. *Sci. Rep.* **2015**, *5*, 1−8.
(31) Poulin, R.; Wechter, R. S.; Pegg, A. E. An Early Enlargement of the Putrescine Pool Is Required for Growth in L1210 Mouse Leukemia Cells under Hypoosmotic Stress. *J. Biol. Chem.* **1991**, *266* (10), 6142−6151.
(32) Tabor, C. W.; Tabor, H. Polyamines. *Annu. Rev. Biochem.* **1984**, *53* (1), 749−790.
(33) Viceps-Madore, D.; Chen, K. Y.; Tsou, H.-R.; Canellakis, E. S. Studies on the Role of Protein Synthesis and of Sodium on the Regulation of Ornithine Decarboxylase Activity. *Biochim. Biophys. Acta, Gen. Subj.* **1982**, *717* (2), 305−315.
(34) Mazia, D.; Schatten, G.; Sale, W. Adhesion of Cells to Surfaces Coated with Polylysine. Applications to Electron Microscopy. *J. Cell Biol.* **1975**, *66* (1), 198−200.
(35) Coskun, A. F.; Cetin, A. E.; Galarreta, B. C.; Alvarez, D. A.; Altug, H.; Ozcan, A. Lensfree Optofluidic Plasmonic Sensor for Real-Time and Label-Free Monitoring of Molecular Binding Events over a Wide Field-of-View. *Sci. Rep.* **2015**, *4*, 1−7.
(36) Barnes, W. L. Surface Plasmon-Polariton Length Scales: A Route to Sub-Wavelength Optics. *J. Opt. A: Pure Appl. Opt.* **2006**, *8* (4). S87.
(37) Cetin, A. E.; Etezadi, D.; Galarreta, B. C.; Busson, M. P.; Eksioglu, Y.; Altug, H. Plasmonic Nanohole Arrays on a Robust Hybrid Substrate for Highly Sensitive Label-Free Biosensing. *ACS Photonics* **2015**, *2* (8), 1167−1174.
(38) Cetin, A. E.; Mertiri, A.; Huang, M.; Erramilli, S.; Altug, H. Thermal Tuning of Surface Plasmon Polaritons Using Liquid Crystals. *Adv. Opt. Mater.* **2013**, *1* (12), 915.

https://doi.org/10.1021/acsnano.1c04031
ACS Nano 2021, 15, 10710−10721